Interpreting the direction of the gravity gradient tensor eigenvectors: The main tidal force and its relation to the curvature parameters of the equipotential surface.

Carlos Cevallos*
CGG
1 Ord Street, West Perth, WA
Carlos.Cevallos@CGG.com

SUMMARY

Rotating the gravity gradient tensor about a vertical axis by an appropriate angle allows one to express its components as functions of the curvatures of the equipotential surface. The description permits the identification of the gravity gradient tensor as the Newtonian tidal tensor and part of the tidal potential. The identification improves the understanding and interpretation of gravity gradient data. With the use of the plunge of the eigenvector associated with the largest eigenvalue or plunge of the main tidal force, it is possible to estimate the location and depth of buried gravity sources; this is illustrated in model data and applied to FALCON airborne gravity gradiometer data from the Canning Basin, Australia.

Key words: Gravity, gradient, tensor, eigenvectors, curvatures.

INTRODUCTION

Curvature of surfaces has been used to interpret geophysical data since the publication of Roberts (2001). Phillips et al. (2007), Cooper and Cowan (2009), Cooper (2010) and Lee et al. (2013) have applied the concept of curvatures to estimate source location, depth and strike from potential field data.

Curvatures of equipotential surfaces and their application to gravity gradiometry are well known; they are a function of the gravity and the gravity gradients and can be applied to interpret gravity gradients in geophysical applications (Cevallos et al., 2013; Chowdhury and Cevallos, 2013; Li and Cevallos, 2013; Cevallos, 2014; Li, 2015).

It was first noticed by Pedersen and Rasmussen (1990) that for a point source, one of the eigenvectors of the gravity gradient tensor points towards it. Later, Beiki and Pedersen (2010) developed a new method, using the eigenvectors of the gravity gradient tensor, to estimate the position of a source body as well as its strike direction. They found out that for a given measurement point, the eigenvector corresponding to the maximum eigenvalue points approximately toward the centre of mass of the causative body. Martinez et al. (2015) building upon the approach by Beiki and Pedersen (2010), similarly utilize an eigenvector based method to generate an accumulation volume representing the depths to anomalous masses to constrain gravity gradient inversions.
The purpose of this paper is to describe the physical meaning of the eigenvectors of the gravity gradient tensor and to show how the direction of the eigenvector associated with the largest eigenvalue can be used in interpretation. In this paper I present the basic, required definitions as proposed by Pedersen and Rasmussen (1990) together with geodetic results from Marussi (1979), illustrate the main properties of the quantity of interest when applied to synthetic data and discuss the application of the method to field data.

THEORY

Defining the potential field as a function of position $\Phi = \Phi(x, y, z)$ in the three orthogonal directions x, y, and z; the gravity field vector is then represented by a three dimensional vector Φk: (k = x, y, z) and the gravity gradient tensor by a matrix Φij: (i, j = x, y, z) where the subscripts indicate partial differentiation with respect to the subscripted variable.

$$\Theta = \begin{pmatrix} \Phi_{xx} & \Phi_{xy} & \Phi_{xz} \\ \Phi_{yx} & \Phi_{yy} & \Phi_{yz} \\ \Phi_{zx} & \Phi_{zy} & \Phi_{zz} \end{pmatrix} \quad (1)$$

The gravity gradient tensor is symmetric, that is, $\Phi ij = \Phi ji$, and its trace is zero, that is, $\Phi xx + \Phi yy + \Phi zz = 0$.
It is always possible to rotate the coordinate system around the z axis with a rotation matrix of the form (Condi, 1999; Dransfield, 1994)

$$R = \begin{pmatrix} \cos\theta & -\sin\theta & 0 \\ \sin\theta & \cos\theta & 0 \\ 0 & 0 & 1 \end{pmatrix} \tag{2}$$

the rotation angle θ defined by (Condi, 1999; Dransfield, 1994)

$$\tan(2\theta + n\pi) = \frac{-2\Phi_{xy}}{\Phi_{xx} - \Phi_{yy}} \text{ , n an integer,} \tag{3}$$

such that in the rotated coordinate system (x', y', z') (z' = z) the rotated Θ' has the form

$$\Theta' = \begin{pmatrix} \Phi'_{xx} & 0 & \Phi'_{xz} \\ 0 & \Phi'_{yy} & \Phi'_{yz} \\ \Phi'_{zx} & \Phi'_{zy} & \Phi'_{zz} \end{pmatrix}, \tag{4}$$

the rotated terms can be identified with

$$\Theta' = -\Phi z \begin{pmatrix} K_{max} & 0 & f_1 \\ 0 & K_{min} & f_2 \\ f_1 & f_2 & -(K_{max} + K_{min}) \end{pmatrix} \tag{5}$$

where Kmax and Kmin are the principal curvatures of the equipotential surface and f1 and f2 the gravity field line curvature components (Cevallos et al. 2013) such that

$$Kmax = -\Phi'xx/\Phi z,\ Kmin = -\Phi'yy/\Phi z,\ f1 = -\Phi'xz/\Phi z \text{ and } f2 = -\Phi'yz/\Phi z. \tag{6}$$

In gravitation theory the negative of the gravity gradient tensor (– Φ) is known as the Newtonian tidal tensor or the tidal tensor (Luminet, 1986; Masi, 2007; Duc and Renaud, 2013) and the expression

$$T = (1/2)\Phi ijxixj = -(1/2)\Phi z[\Phi 11x12 + \Phi 22x22 + \Phi 33x32 + (\Phi 12 + \Phi 21)x1x2 + (\Phi 13 + \Phi 31)x1x3 + (\Phi 23 + \Phi 32)x2x3] \tag{7}$$

where x1 = x, x2 = y and x3 = z, is the tidal potential used in geodetics (Marussi, 1979). In this case substitution yields

$$T = (-\Phi z/2)\ [Kmaxx2 + Kminy2 - (Kmax + Kmin)z2 + 2f1xy + 2f2yz] \tag{8}$$

This allows the eigenvectors of Θ' to be identified as the tidal axes with directions given by (Marussi, 1979):

$$\tan 2\zeta = \frac{f_1^2}{(\lambda - K_{max})^2} + \frac{f_2^2}{(\lambda - K_{min})^2} \tag{9}$$

and

$$\tan\alpha = \frac{f_2(\lambda - K_{max})}{f_1(\lambda - K_{min})} \tag{10}$$

where ζ and α are the angles that the eigenvectors make with z' and x' respectively, and λ is an eigenvalue of Θ' or Θ (Θ' and Θ have the same eigenvalues).

These identifications give meaning to the eigenvectors of Θ. For example, we can now look at the schematics of the eigenvectors above the centre of a pseudo 2D body displayed in Figure 1 of Beiki and Pedersen (2010) where V1, V2 and V3 are the eigenvectors associated with the maximum, intermediate and minimum eigenvalues of Θ and understand why V1 is pointing towards the centre of mass of the body at the displayed observation point: it is the direction of the main tidal force.

The direction of an eigenvector can be split into a plunge (π/2 – ζ) and a plunge direction (α). I have found the plunge of the eigenvector associated with the largest eigenvalue (plunge of the main tidal force) useful in interpretation as it gives an immediate idea of location and depth of the sources of the gravity field.

MODELING

Visualization of the horizontal variations of the plunge and the plunge direction of the main tidal force can be achieved using synthetic models of the type used in Cevallos et al. (2013). In the first model, two 1 km3 model cubes were assigned density contrasts of ± 1.0 × 103 Kg/m3 respectively in a 2.67 × 103 Kg/m3 background density. The cubes are separated by 1 km and have a depth to top of 100 m.

The plunge and the plunge direction of the main tidal force (Figure 2 and Figure 3) show the classical behaviour of this force: it points towards the centre of the more dense body on the left and away from the centre of the less dense body on the right except

when above or near the centre of symmetry. As for the curvature attributes of generic equipotential surfaces a symmetry or an anti-symmetry would be expected, it may come as a surprise that the result of this modelling does not show an East West symmetry or anti symmetry (Cevallos et al. 2013); this is explained by the fact that tidal forces are a consequence of gravity forces that are only attractive. Figure 2 shows that in this particular case the effect of the denser body is mostly absent in the eastern half of the area; this is because its effect is mostly cancelled by the effect of the less dense body. Figure 3 shows that if we think of the direction of the main tidal force as an arrow in space, then the pattern resembles that of an electric or a magnetic dipole: arrows starting at the less dense body and ending at the denser body.

In a second set of models both 1 km3 model cubes were assigned a density contrast of + 1.0 × 103 Kg/m3 in a 2.67 × 103 Kg/m3 background density. The cubes are separated by 1 km and the western body has a fixed depth to top of 100 m and the second body has depths to top of 100 m, 600 m and 1100 m. Figures 4a, 4b and 4c; 5a, 5b and 5c; 6a, 6b and 6c; show Φzz (1 Eötvös = 10-9/s2), the largest eigenvalue and the plunge of the main tidal force for each set of models respectively.

Figures 4a, 4b and 4c show the typical characteristics of Φzz: larger values centred over the bodies and decrease quickly with depth. Figures 5a, 5b and 5c show that that the largest eigenvalue is not as good as Φzz in positioning the bodies and their centres. Figures 6a, 6b and 6c show typical characteristics of the tidal force (they are easier to understand in terms of astrophysics); in general they are not good at defining edges but good at positioning the bodies.

In particular, Figure 6a shows a "neutral zone" that at its ends has two small zones in which the plunge of the main tidal force points to the centre of mass of the two bodies instead of just one, this zone gradually disappears from the images (Figures 6b and 6c) as it goes deeper; the change in position of the joint centre of mass has the additional consequence that over the deepest body the plunge of the main tidal force does not attain the 90 degree value.

An important result that can be observed from Figures 4c, 5c and 6c is that the plunge of the main tidal force image defines deeper features better than the Φzz and the largest eigenvalue images.

In general, a good idea of the approximate depths of the centres of mass of the bodies may be achieved by observing the lateral behaviour (horizontal gradient) and the value of the plunge of the main tidal force. For example, for isolated bodies with a positive density contrast (denser than its surroundings) (Figures 2, 6a, 6b and 6c) the depth to their centres of mass can be estimated in several ways: the simplest one involves using the 45 degree contour and dividing its "width" by two. This calculation would be very similar to the one done in the tilt depth method (Miller and Singh, 1994; Verduzco et al., 2004; Salem et al. 2007) and in the adaptive tilt angle method (Salem et al., 2013). These methods are not related to the present one as this method uses all the components of the tensor, calculates eigenvectors and does not assume any type of sources.

The width of the 45 degree contour could be estimated in different ways, for example: Taking the average of the shortest and longest widths (or several widths) or calculating the perimeter of the contour and diving by π. These two methods would work well for isolated anomalies but for compound anomalies because of interference effects they would tend to underestimate the depth of sources (especially the deeper ones).

In general, a better estimation is obtained by measuring the distance from the horizontal location of the approximate centre of mass (point of maximum plunge) to the 45 degree contour as far away as possible from interference zones. Figure 7 shows the proposed procedure: The depth estimations (length of blue dots line) yield 620 m and 1575 m for the shallow and deep synthetic model cubes (actual depths to centres of mass: 600 m and 1600 m). This last method is not straightforward; the depth estimate is directly a half width and requires some care in picking for each individual anomaly which point in its associated 45 degree contour to use.

There are less simple or "complete" ways of estimating the depth to centres of mass like using other contours or all contours and possibly variable size moving windows adjusted to the "size" of anomalies. Simple methods can be done quickly and graphically. If more detail or need to separate neighbouring sources is required, the much more sophisticated eigenvector based methods of Martinez et al. (2015) and Beiki and Pedersen (2010) can be used. The advantage of using the plunge of the main tidal force is that, in many cases, depth to centres of mass of sources can be estimated by inspection.

APPLICATION

The plunge of the main tidal force was calculated for the FALCON® AGG data from the King Sound area of the Canning Basin, Western Australia (Cevallos et al. 2013; Cevallos, 2014; Kovac et al, 2013) (Figure 8). The plunge of the main tidal force was assessed using an independent geological interpretation based on Φzz, 2D seismic sections and interpreted horizons, a depth to magnetic basement surface and well logs (Kovac et al, 2013).

King Sound is located on the southern margin of the Lennard shelf, on the northern flank of the Canning basin. The King Sound area consists of Archaean to Proterozoic basement overlain by Palaeozoic and Mesozoic sedimentary fill. In the Late Devonian and Early Carboniferous period, the elevated fault controlled basement in the north was rimmed by carbonate reefs and carbonate breccias, while in the south; siliciclastic submarine fan deposits and turbidites have been deposited along the fault controlled margin of the basement in a deep marine environment. Based on the relative amplitudes of the AGG responses and detailed 2½D gravity modelling, three main lithological units were identified: The Fairfield Group carbonates were interpreted to be high density sources. Fore reef debris and carbonate clastics re deposited from carbonates higher up the slope and/or from the carbonate platform were interpreted to be medium density sources. Turbidites, debris flows and associated clastic basinal sequences were interpreted as low density sources.

Figures 9, 10 and 11 show the geological interpretation over the Φzz, the shape index and the plunge of the main tidal force images. Comparisons show some general results: the plunge of the main tidal force offers information not readily derivable from any curvature or the shape index of the equipotential surfaces (Cevallos et al. 2013); it is worse at defining boundaries than other curvature attributes but better at distinguishing small to intermediate bodies from each other or as isolated features and defines large bodies at different positions. As it uses all the gradients it has more high spatial frequency content than any particular gradient or the shape index and in this case it offers the result that in areas of interest within the carbonates the trends of the centres of mass are different from both the trends of the maximum values of Φzz and the dome trends of the shape index. This is valuable information as it strongly influences carbonate targeting strategies.

In the King Sound study area, interpretation of intrasedimentary structure and basement architecture was completed using an integration of AGG, magnetic, 2 D seismic and well data (Kovac et al, 2013). Figure 12 shows the position of seismic line F81A–454 and the relevant wells over the background image of the plunge of the main tidal force with its 45 degree contour and Figure 13 shows the interpreted seismic line F81A–454. Two petroleum exploration wells exist at King Sound: Esso, Puratte 1; and Command Petroleum, Padilpa 1 (Figure 12). The Padilpa 1 well penetrated sedimentary layers until it met a gabbroid intrusion at depth of 2172 m and was stopped at a depth of 2184 m. Figure 14 shows the southeast corner of the King Sound study area. In it, the possible depth estimations to the depth of the centre of mass of the body under Padilpa 1 are drawn from the position of the well to the positions of the nearest different parts of 45 degree contour: starting from the southwest and going counterclockwise they yield 2424 m, 3013 m, 2910 m, 1751 m and 2814 m; as all the parts of the contour except the one to the southwest of the well look like they are enclosing neutral zones and the better estimations are obtained by measuring the distance from the horizontal location of the approximate centre of mass (point of maximum plunge) to the 45 degree contour as far away as possible from interference zones, then the best depth estimation is 2424 m. Obviously, the centre of mass of the gabbro intrusion must be below 2172 m, and from Figure 13 it can be seen that adding 10% of the total depth (217 m) is not unreasonable. This addition suggests a total depth of 2389 m that compares favourably with the estimation.

CONCLUSIONS

The gravity gradient tensor can be expressed in terms of curvature components. The concept of tidal tensor gives meaning to the eigenvalues and eigenvectors of the gravity gradient tensor.

Using the plunge of the main tidal force for individual bodies with distinct gravity anomalies and sets of bodies that have compound gravity anomalies offers the interpreter the horizontal positions of the approximate centres of mass, better definition with depth of these and their approximate depth estimations. The calculation of the plunge of the main tidal force is direct and it does not require creating windows to do calculations for subsets of data, minimization procedures or clustering techniques. If more precise estimations of depth are needed eigenvector based methods to generate an accumulation volume representing the depths to anomalous masses can be used in order to create a representative depth volume. Obviously, in complex situations (many sources interacting), the plunge of the main tidal force by itself cannot be used to distinguish an excess of mass from a deficiency of mass in source bodies, other information is needed like the one provided from the plunge direction or Φzz to determine this.

The directions of the eigenvectors of the gravity gradiometry tensor can be identified as the tidal axes. This can be used not only in locating geological bodies or inversions schemes but also in interpretation. The plunge of the main tidal force can be used to position the approximate centres of mass of sources. Its horizontal changes can be used to obtain an estimation of the depth of those approximate centres of mass.

REFERENCES

Beiki, M., and L. B. Pedersen, 2010, Eigenvector analysis of gravity gradient tensor to locate geologic bodies: Geophysics, 75, I37–I49.

Cevallos, C., P. Kovac, and S. J. Lowe, 2013, Application of curvatures to airborne gravity gradiometry data in oil exploration: Geophysics, 78, 4, G81–G88.

Cevallos, C., 2014, Automatic generation of 3D geophysical models using curvatures derived from airborne gravity gradient data: Geophysics, 79, 5, G49–G58.

Chowdhury, P. R., and C. Cevallos, 2013, Geometric shapes derived from airborne gravity gradiometry data: New tools for the explorationist: The Leading Edge, 32, 1468–1474.

Condi, F. J., 1999, Estimating Subsurface Structure through Gravity and Gravity Gradiometry Inversion: PhD Thesis, Rice University.

Cooper, G. R. J., 2010, Enhancing Ridges in Potential Field Data: Exploration Geophysics, 41, 170–173.

Cooper, G. R. J., and D. R. Cowan, 2009, Terracing Potential Field Data: Geophysical Prospecting, 57, 1067–1071.

Dransfield, M. H., 1994, Airborne Gravity Gradiometry: PhD Thesis, The University of Western Australia, Appendix B.

Duc, P. A., and F. Renaud, 2013, Tides in Colliding Galaxies in Souchay, J., Mathis, S. and T. Tokeida, eds., 2013: Tides in Astronomy and Astrophysics, 337–338.

Kovac, P., S. Lowe, T. Rudge, C. Cevallos, J. Feijth, and L. Brett, 2013, Basement architecture from high-resolution gravity gradient, magnetic, and seismic data, King Sound, Canning Basin, Western Australia: AAPG Bulletin, 97, 1597–1620.

Lee, M. D., W. A. Morris, G. Leblanc, and J. Harris, 2013, Curvature analysis to differentiate magnetic sources for geologic mapping: Geophysical Prospecting, 61, (S1), 572–585.

Li, X., and C. Cevallos, 2013, Curvature of the equipotential surface, gravity potential, field and gradient anomalies: 83rd Annual International Meeting, SEG, Expanded Abstracts, 1180–1184.

Li, X., 2015, Curvature of a geometric surface and curvature of gravity and magnetic anomalies: Geophysics, 80, 1, G15–G26.

Luminet, J. P., 1986, Tidal Disruption in Carter, B. and J. B. Hartle, eds., Gravitation in Astrophysics, Cargèse. NATO ASI Series B, 156, 215–217.

Martinez, C., D. Wedge, Y. Li, and E.-J. Holden, 2015, Constraining gravity gradient inversion with a source depth volume: 24th International Geophysical Conference and Exhibition, ASEG Extended Abstracts, 1–4.

Marussi, A., 1979, The tidal field of a planet and the related intrinsic reference systems: Geophys. J. R. astr. Soc., 56, 409–417.

Masi, M., 2007, On compressive radial tidal forces: Am. J. Phys., 75(2), 116–124.

Miller, H. G., and V. Singh, 1994, Potential field tilt – A new concept for location of potential field sources: Journal of Applied Geophysics, 32, 213–217.

Pedersen, L. B., and T. M. Rasmussen, 1990, The gradient tensor of potential field anomalies: Some implications on data collection and data processing of maps: Geophysics, 55, 1558–1566.

Phillips, J. D., R. O. Hansen, and R. J. Blakely, 2007, The use of curvature in potential field interpretation: Exploration Geophysics, 38, 111–119.

Roberts, A., 2001, Curvature attributes and their application to 3D interpreted horizons: First Break, 19, 85–100.

Salem, A., S. Williams, J. D. Fairhead, D. Ravat, and R. Smith, 2007, Tilt depth method: A simple depth estimation using first order magnetic derivatives: The Leading Edge, 26, 1502–1505.

Salem, A., S. Masterton, S. Campbell, J. D. Fairhead, J. Dickinson, and C. Murphy, 2013, Interpretation of tensor gravity data using an adaptive tilt angle method: Geophysical Prospecting, 61, 1065–1076.

Verduzco, B., J. D. Fairhead, C. M. Green, and C. MacKenzie, 2004, New insights into magnetic derivatives for structural mapping: The Leading Edge, 23, 116–119.

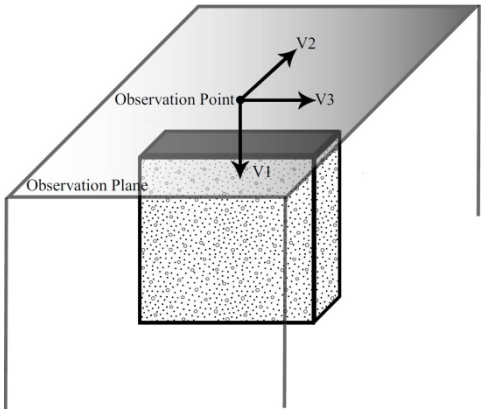

Figure 1. Schematics of the eigenvectors above the centre of a pseudo 2D body (after Beiki and Pedersen, 2010).

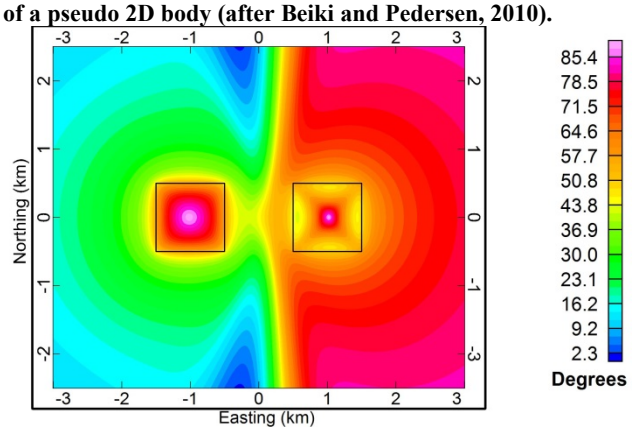

Figure 2. Plunge of the main tidal force over model cubes, shown by the black outlines (denser body on left). Degrees from horizontal, positive down.

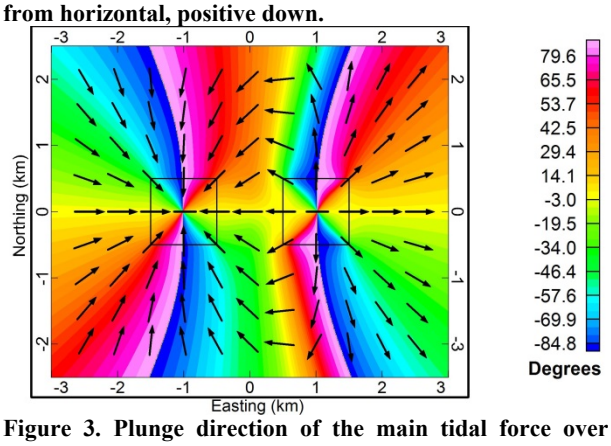

Figure 3. Plunge direction of the main tidal force over model cubes, shown by the black outlines (denser body on left). Degrees from East, positive counter clockwise. Individual directions plotted as black straight arrows at every 500 m.

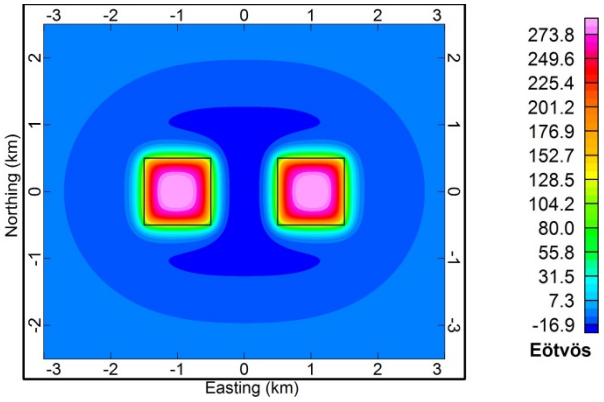

Figure 4a. Φzz over model cubes, shown by black outlines (same depth).

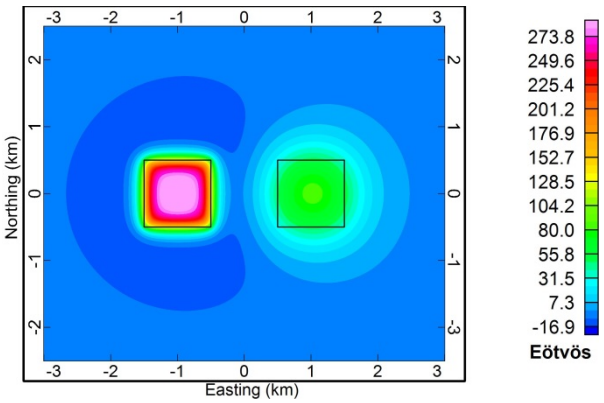

Figure 4b. Φzz over model cubes, shown by black outlines (deeper body on right).

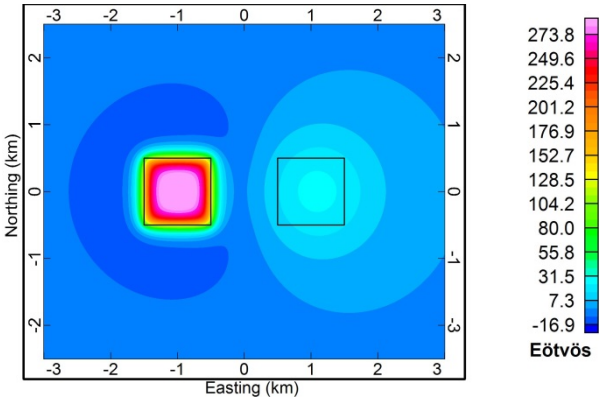

Figure 4c. Φzz over model cubes, shown by black outlines (deepest body on right).

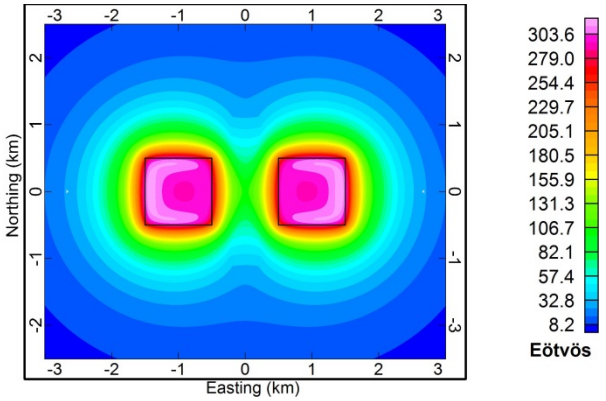

Figure 5a. Largest eigenvalue over model cubes, shown by black outlines (same depth).

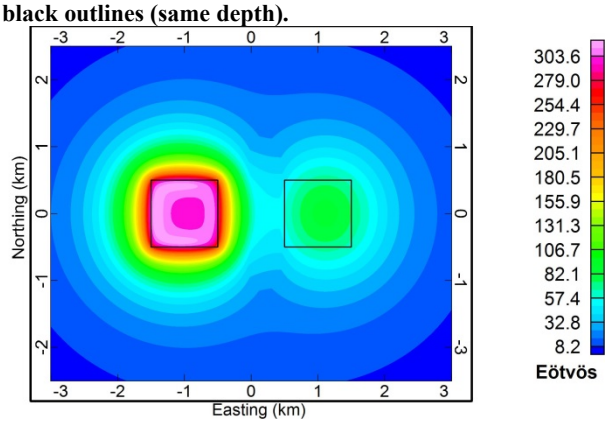

Figure 5b. Largest eigenvalue over model cubes, shown by black outlines (deeper body on right).

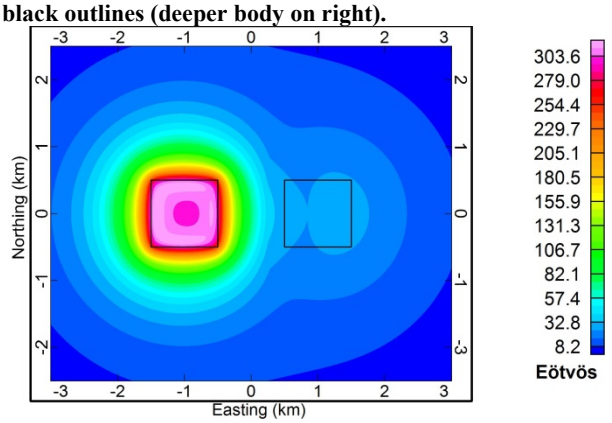

Figure 5c. Largest eigenvalue over model cubes, shown by black outlines (deepest body on right).

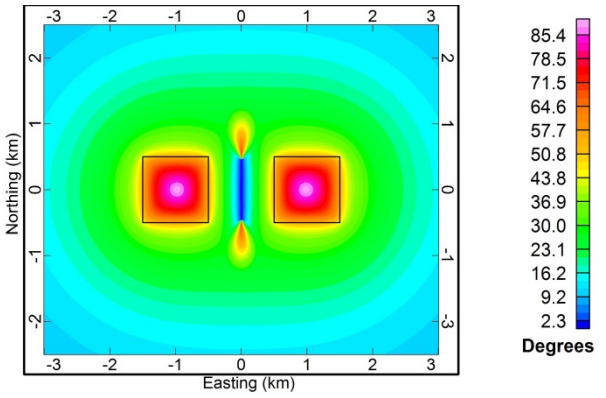

Figure 6a. Plunge of the main tidal force over model cubes, shown by black outlines (same depth).

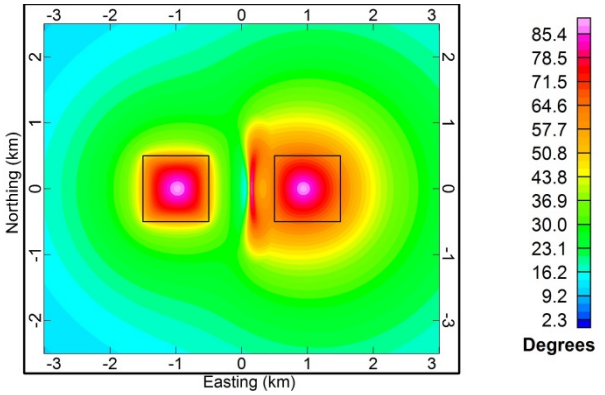

Figure 6b. Plunge of the main tidal force over model cubes, shown by black outlines (deeper model on right).

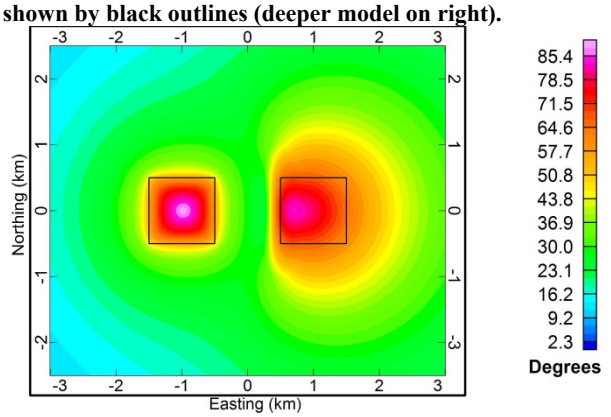

Figure 6c. Plunge of the main tidal force over model cubes, shown by black outlines (deepest model on right).

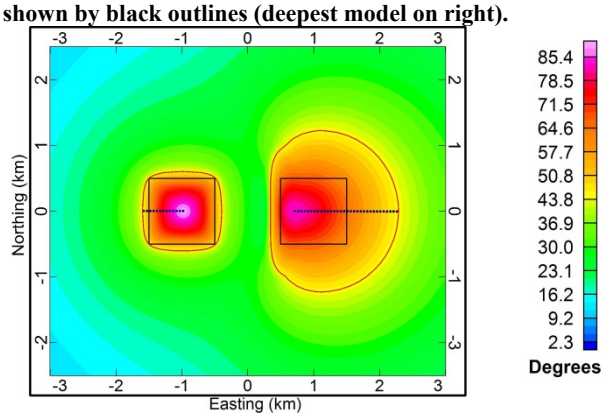

Figure 7. Plunge of the main tidal force over model cubes, shown by black outlines (deepest model on right). Red lines mark the 45 degree contour. Lengths of blue dotted lines estimate depths of centres of mass of synthetic model cubes

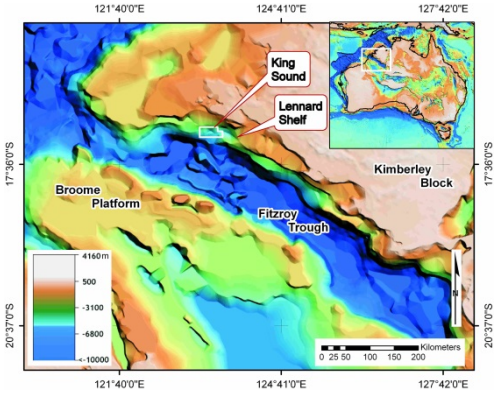

Figure 8. Location of the King Sound survey area (after Kovac et al., 2013).

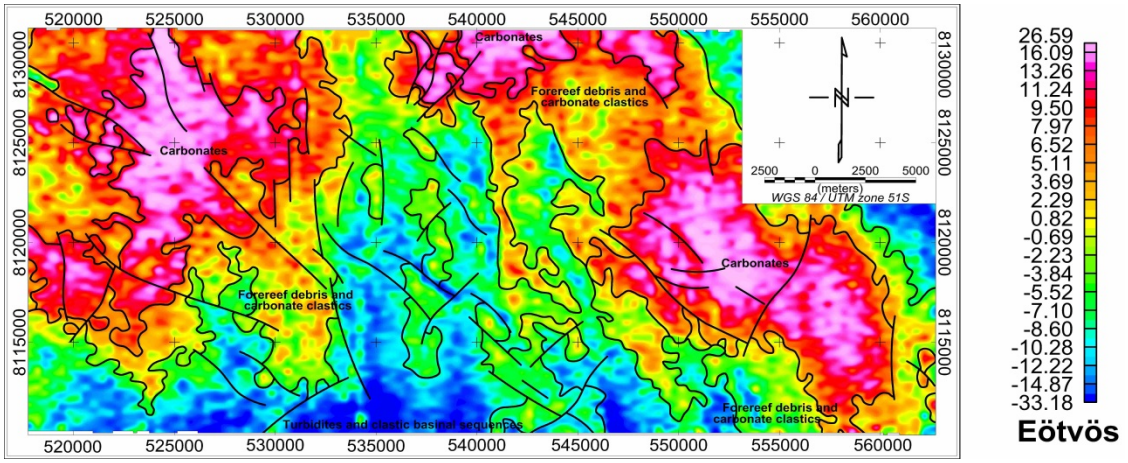

Figure 9. Geologic interpretation (unit boundaries and faults) of gravity gradiometry data over the Φzz image.

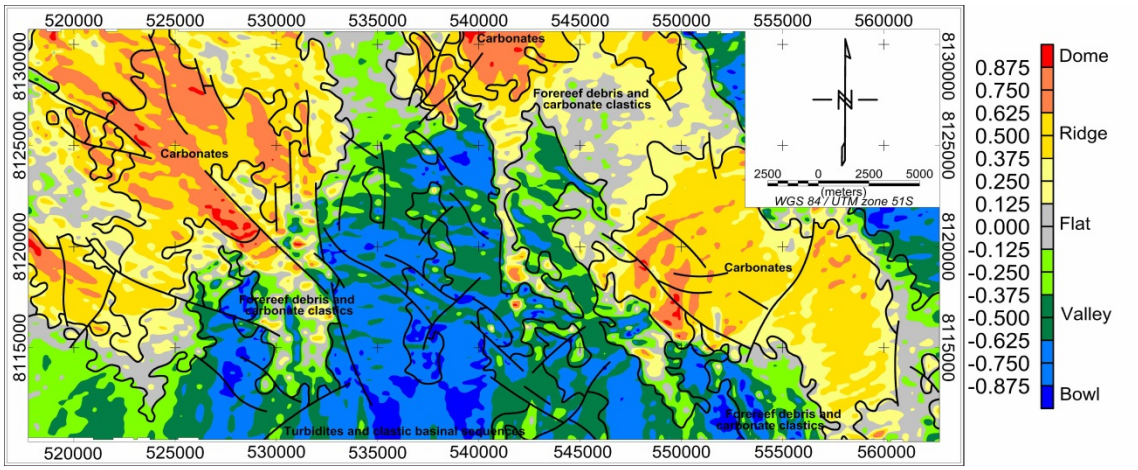

Figure 10. Geologic interpretation (unit boundaries and faults) of gravity gradiometry data over the shape index of the equipotential surfaces image.

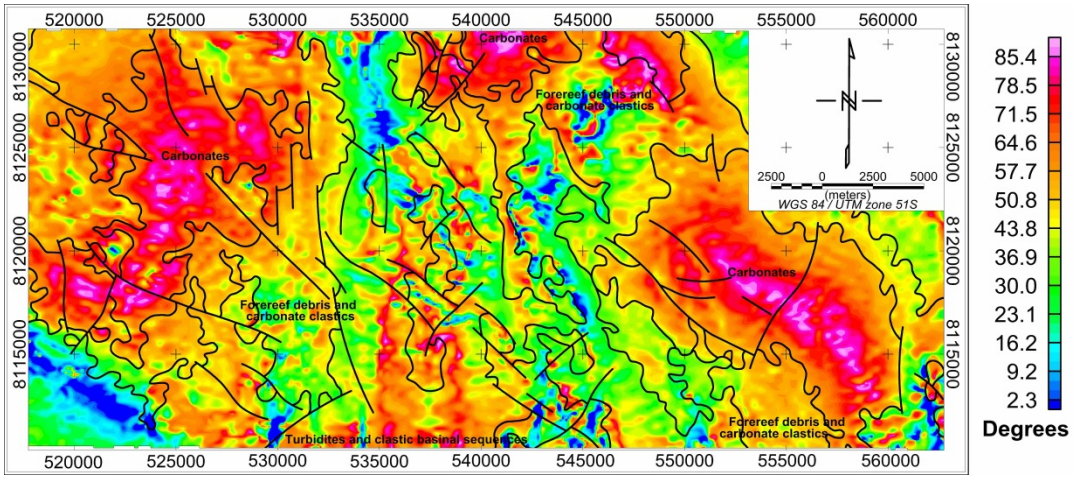

Figure 11. Geologic interpretation (unit boundaries and faults) of gravity gradiometry data over plunge of the main tidal force image. Degrees from horizontal, positive down.

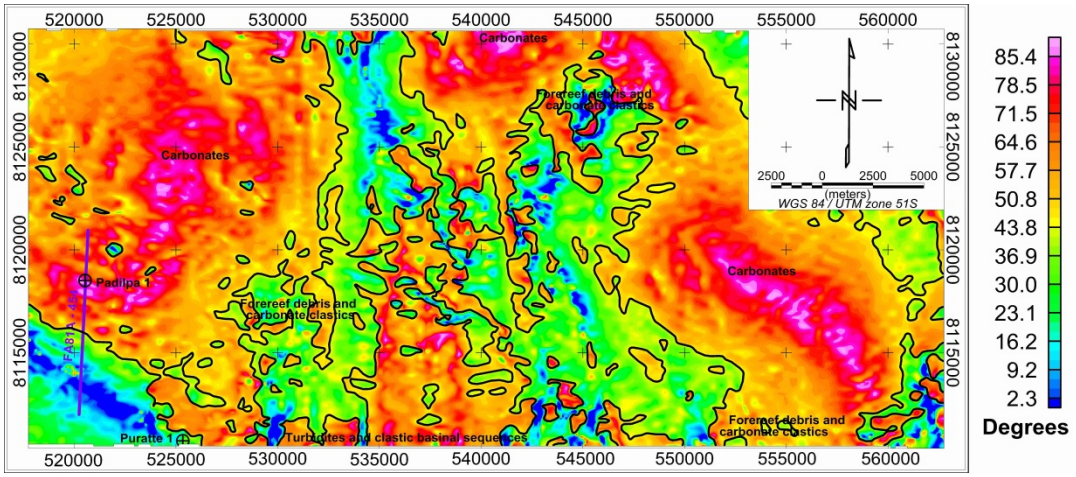

Figure 12. Position of seismic line F81A–454 (purple colour) and Padilpa 1 and Puratte 1 wells over the plunge of the main tidal force (degrees from horizontal, positive down) image with black lines marking the 45 degree contour.

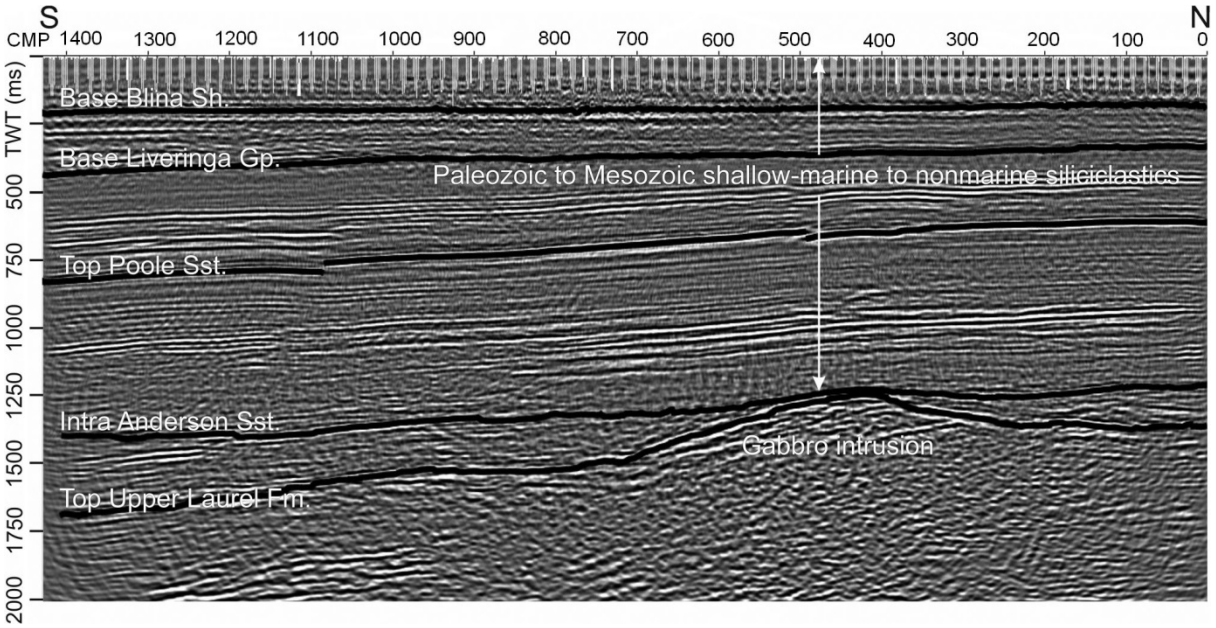

Figure 13. Seismic line F81A-454 with an interpreted gabbroid intrusion drilled by the Padilpa 1 well. For the location of the seismic line, see Figure 12 (after Kovac et al., 2013).

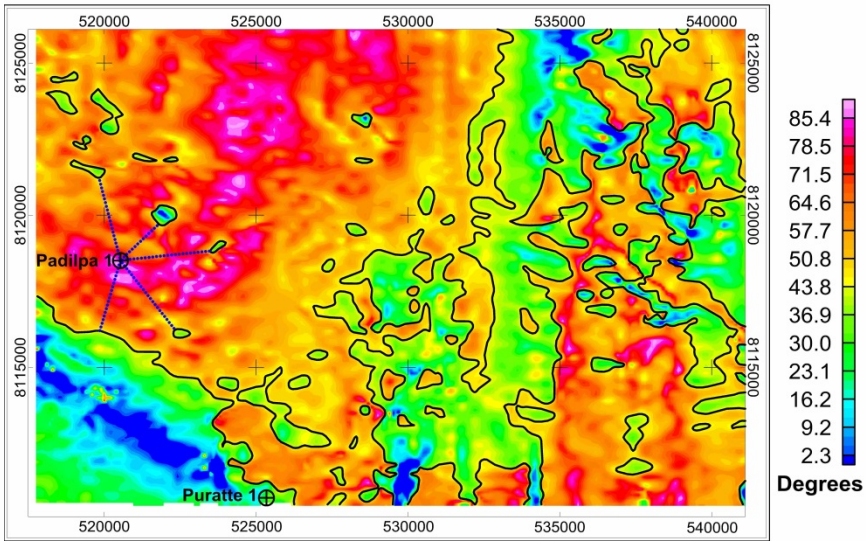

Figure 14. Plunge of the main tidal force (degrees from horizontal, positive down) with black lines marking the 45 degree contour. Lengths of blue dotted lines estimate depth of centre of mass of the body under Padilpa 1.